



## Effect of relativistic equation of state and diffusion coefficient on diffusive shock acceleration

ANSHUMAN VERMA <sup>1</sup>, SAKSHAM CHANDNA,<sup>1</sup> AND RITAM MALICK <sup>1</sup>

<sup>1</sup>*Department of Physics, Indian Institute of Science Education and Research Bhopal,  
Bhopal - 462066, Madhya Pradesh, India*

### ABSTRACT

Diffusive Shock Acceleration, resulting from first-order Fermi acceleration occurring near Magneto-hydrodynamic shock waves, is essential in explaining the power law spectrum in various astrophysical radiation and cosmic rays. We perform Monte Carlo simulations to model the stochastic scattering process in Fermi acceleration, capturing the confinement of particles around the shock within the ambient fluid. The model is tested and validated by comparing it with the spectral index obtained with analytical calculation. Assuming a relativistic EoS, we calculate the power-law spectral index for different diffusion coefficients. With constant diffusion co-efficient and stiffer EoS, the observed range of the spectral index is very narrow; however, as the EoS becomes softer, the range increases. With varying diffusion co-efficient stiffer EoS fails to give a well-defined spectral index (no linear spectrum); however, as the EoS becomes softer, the spectral index lies between 2 – 4. For ultra-relativistic shocks, we consistently obtained a linear spectrum; however, the spectral index range varied considerably with the diffusion coefficient.

*Keywords:* Particle Acceleration — Shock Wave — Monte-Carlo Simulation

### 1. INTRODUCTION

The theory of particle acceleration through shock waves emerged in the late 1970's (Alfvén 1943; Fermi 1949; Krymskii 1977) and has since become the dominant framework for understanding astrophysical particle acceleration. A universal feature of high-energy astrophysical phenomena (such as Supernova remnants (SNRs), Gamma-Ray bursts (GRBs) and Active Galactic Nuclei (AGNs)) is the release of highly-relativistic particles from them (Bell 1978; Blandford & Ostriker 1978). These particles are accelerated to high energies near these energetic environments and thrown across the Universe, forming cosmic radiation (Prishchep & Ptuskin 1981; Berezhko et al. 2002). These particles are either detected directly as cosmic radiation or indirectly in the form of non-thermal radiation. The synchrotron emission and inverse Compton radiation from the accelerated electrons exhibit a power-law energy spectrum in specific energy ranges (Blandford & Eichler 1987). The cosmic ray spectrum obtained through various experimental ventures is displayed in many literature (Longair 2011). The “knee” of the spectrum is observed around the  $PeV$  energy range, where a steepening of the spectral curve is seen. This feature probably corresponds to the upper end of Galactic Cosmic Rays (GCRs) (Gaisser 2006). In lower energy ranges, from  $GeV$  to  $TeV$ , most of the observed GCRs seem to originate in regions around a particular class of supernova explosions, which involve rapid evolution and collapse of massive progenitor stars (Wolf-Rayet stars) (Biermann et al. 2019). The highest energies for GCRs are thought to emerge from strong magnetic fields in the acceleration region near Sedov-Taylor blast waves in SNRs (Schure et al. 2012). Beyond the “knee” of the spectrum, primarily extra-galactic sources are thought to be responsible. Our focus is mainly on the power-law energy spectrum observed before the “knee” of the spectrum, where sources and production mechanisms are

more easily identifiable using the diffusive shock acceleration (DSA) model (Aartsen et al. 2013; Apel et al. 2014). For  $E < 10^{15} eV$ , the power-law energy distribution:  $N_{obs}(E)dE \propto E^{-2.7}dE$  is observed (Adriani et al. 2014; Aguilar et al. 2015; Neronov, Andrii et al. 2017). In non-thermal radio sources like SNRs and radio galaxies, synchrotron emission by  $GeV$  electrons also gives a similar energy spectrum, where the power law exponent  $s$  ranges between  $s \approx 2 - 2.7$  (Yang et al. 2014; Acero et al. 2015; Neronov & Malyshev 2015). The source spectrum is thought to arise from the competition between the energy gained per shock-crossing cycle (in Sedov-Taylor blasts) and the contribution from the probability of plasma particles escaping the acceleration region after each collision cycle (Achterberg et al. 2001a; Gaisser 2006).

The DSA mechanism, initially proposed by Fermi, involves stochastic scattering of plasma particles by Alfvén waves near collisionless shock fronts. This scattering confines particles near the shock, allowing for prolonged acceleration (Fermi 1949; Bell 1978; Drury 1983; Kirk & Dendy 2001). DSA occurs when the relative upstream fluid velocity exceeds the downstream velocity (in the rest frame of the shock). As particles cross the shock, they encounter the relative motion of fluid regions on either side of the shock, leading to energy gains through Fermi acceleration (Bell 2004). The interplay between energy gain from shock crossings and the likelihood of particles moving downstream generates a power-law spectra. Magnetic field irregularities around the shock confine particles near the shock front. In non-relativistic cases, an isotropic particle velocity distribution is assumed due to scattering, forming the basis for many DSA analyses (Bell 2004; Schure et al. 2012). In relativistic shocks, anisotropic particle velocity distributions arise due to comparable velocities of the bulk plasma and individual particle velocities (Achterberg et al. 1994; Yoon et al. 2011, 2017; Abeyssekara et al. 2019; Yuan et al. 2020). Additionally, the orientation of magnetic field lines relative to the shock normal influences the spectral index. Thus, for relativistic shock acceleration, semi-analytic or numerical models are suitable to determine the spectral index (Kirk & Schneider 1987a,b; Axford et al. 1977; Kirk & Schneider 1987a,b; Ballard & Heavens 1991; Achterberg et al. 2001a,b; Gallant 2002).

The DSA problem can be tackled through two main approaches: macroscopic and microscopic. The microscopic approach tracks individual particle motion near a shockwave and analytically derives a spectral index value of  $s = 2$  for non-relativistic strong parallel shocks in a diffuse medium (Bell 1978; Allen & Tildesley 1989). The macroscopic approach solves the transport equation for upstream and downstream regions of non-relativistic shocks, matching solutions at the shock discontinuity (Blandford & Ostriker 1978). For relativistic shock scenarios, (Peacock 1981) and (Kirk & Schneider 1987a,b) adopted microscopic approaches similar to Bell's, considering the competition between particle acceleration in converging flows of scattering centres and escape into the downstream region, resulting in power-law spectra. Gallant reviewed theoretical aspects of particle acceleration with ultra-relativistic and moderately relativistic shocks (Gallant 2002). However, these theoretical approaches often struggle to describe the spectral index values in more realistic DSA cases comprehensively. A realistic treatment of the DSA problem necessitates solving the corresponding Fokker-Planck type equation for particles (Risken 1989; Arzner & Vlahos 2004; Arzner et al. 2006).

To simulate such a scenario, we have adopted an ultra-relativistic equation of state and incorporated various diffusion coefficients in the Monte-Carlo simulations to estimate the spectral indices of the particle spectrum. The input parameters for the simulation code include the bulk velocity values  $u_u$  (upstream) and  $u_d$  (downstream), measured in the shock rest frame, which determines the specific type of shock under consideration. A shock is considered relativistic if the  $u_u$  value is relativistic, while it is classified as non-relativistic if the  $u_u$  value is non-relativistic. The relationship between  $u_u$  and  $u_d$  is defined by the shock jump conditions (Landau & Lifshitz 1987; Csernai 1994; Mallick & Irfan 2019).

The paper is structured as follows: In Section II, we delve into the formulations, covering the derivation of the energy spectrum, the theory of shock waves, the transport equation, and the establishment of the Monte-Carlo model. Section III outlines the step-by-step procedures for the Monte-Carlo simulations. Section IV presents our results, demonstrating various scenarios by considering an ultra-relativistic equation of state with different diffusion coefficients. Finally, Section V summarises our findings and concludes the study.

## 2. FORMALISM

### 2.1. The Energy Spectrum

DSA is characterized by two parameters: the average ratio of energies before and after a particle crosses the shock twice and the probability of a particle remaining in the acceleration region after a single shock crossing cycle. The average final energy of a particle with initial energy  $E_0$  after a single shock crossing cycle is given as  $E = \beta E_0$ , ( $\beta$  a

constant). The probability of the particle being confined near the shock wave due to scattering by Alfvén waves after the particle crosses the shock twice instead of escaping into the downstream region is  $P_r$ .

After  $k$ th shocks cross, the average final energy of a particle is given by

$$E = \beta^k E_0 \quad (1)$$

The final average number density of particles ( $N$ ) still present in the acceleration region after  $k$  crossing cycles is

$$N = P_r^k N_0 \quad (2)$$

where  $N_0$  is the initial number density of particles in the acceleration region.

Simplifying, we have

$$\frac{N}{N_0} = \left( \frac{E}{E_0} \right)^{\frac{\ln(P_r)}{\ln(\beta)}} \quad (3)$$

Differentiating equation 3 with respect to  $E$ , and noting  $dN(\geq E) = N(\geq (E+dE)) - N(\geq E) = N(dE) = N(E)dE$ :

$$N(E)dE = \text{const} \times E^{-1 + \left(\frac{\ln P_r}{\ln \beta}\right)} dE \quad (4)$$

$$\implies N(E)dE \propto E^{-s} dE \quad (5)$$

This gives the emergence of the power-law energy spectrum of DSA where  $s$  being the spectral index of power-law for equation.

## 2.2. Shock Waves

DSA occurs when the relative upstream fluid velocity exceeds the downstream velocity with respect to the shock. As particles cross the shock, they encounter the relative motion of fluid regions on either side, leading to energy gains through Fermi acceleration.

The velocities of the upstream and downstream matter is given by (Mallick & Irfan 2019)

$$\frac{u_u^2}{c^2} = \frac{(p_d - p_u)(\epsilon_d + p_u)}{(\epsilon_d - \epsilon_u)(\epsilon_u + p_d)} \quad (6)$$

$$\frac{u_d^2}{c^2} = \frac{(p_d - p_u)(\epsilon_u + p_d)}{(\epsilon_d - \epsilon_u)(\epsilon_d + p_u)} \quad (7)$$

Solving the above equation the relation between the velocities is given by

$$\frac{u_u u_d}{c^2} = \frac{(p_u - p_d)}{(\epsilon_u - \epsilon_d)} \quad (8)$$

In strong shocks,  $p_d \gg p_u$  and  $\epsilon_d \gg \epsilon_u \implies u_d \ll u_u$ . Under these conditions, velocities takes the form as

$$u_u \rightarrow c ; u_d \rightarrow \frac{c}{n} \quad (9)$$

## 2.3. The Transport equation

The transport equation relevant for the problem is given by

$$\Gamma(1 + v\mu \frac{u}{c^2}) \frac{\partial f}{\partial t_s} + \Gamma(u + v\mu) \frac{\partial f}{\partial z_s} = \frac{\partial}{\partial \mu} D_{\mu\mu}(P)(1 - \mu^2) \frac{\partial f}{\partial \mu} \quad (10)$$

where  $f = f(p, \mu, z, t)$  is the particle distribution function, which is a function of momentum  $p$ , pitch angle  $\mu = \cos(\theta)$ , the position of the particle  $z_s$  (with respect to shock normal) and  $t_s$  the time.  $D_{\mu\mu}(P)$  is the diffusion co-efficient,  $v$  is the velocity of the particle and  $\Gamma = \sqrt{\frac{1}{1 - \frac{u^2}{c^2}}}$  is the Lorentz factor with respect to  $u$ .

For simplicity, only the solutions of equation 10, which are stationary in the shock rest frame, are considered, i.e.,  $\frac{\partial f}{\partial t_s} = 0$ , so

$$\Gamma(u + \mu) \frac{\partial f}{\partial z_s} = \frac{\partial}{\partial \mu} D_{\mu\mu}(P)(1 - \mu^2) \frac{\partial f}{\partial \mu} \quad (11)$$

This is the transport equation that guides the evolution of pitch-angle in both the upstream and downstream fluid.

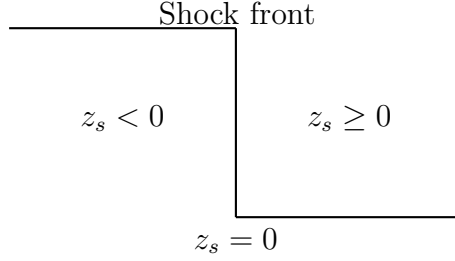


**Figure 1.** A schematic diagram of the shock front serves as a frame of reference, with "z<sub>s</sub>" representing the z-coordinate of the particle position measured in the shock rest frame. In this context, when z<sub>s</sub> < 0, it indicates the upstream (u) region, while z<sub>s</sub> ≥ 0 denotes the downstream (d) matter relative to the shock front.

#### 2.4. Set up for the Monte - Carlo Simulations

For isotropic diffusion, the transport equation becomes

$$\frac{\partial f}{\partial t} = D_{\mu\mu} \frac{\partial}{\partial \mu} (P)(1 - \mu^2) \frac{\partial f}{\partial \mu} \quad (12)$$

In the shock rest frame, the particle travels a distance  $\Delta z_s$  along z direction between two successive deflections, which is given by

$$\Delta z_s = \frac{\mu + u}{1 + \mu u} \Delta t_s = \Gamma(\mu + u) \Delta t' = \Gamma(\mu + u) \frac{\Delta t}{D_{\mu\mu}(P)} \quad (13)$$

This gives how the particle changes its positions per time step between subsequent deflections of pitch-angle. Substituting this in equation 12, we get

$$\frac{\partial f}{\partial(\Delta t)} = \frac{\partial}{\partial \mu} (1 - \mu^2) \frac{\partial f}{\partial \mu} \quad (14)$$

An inherent issue arises with equation 13 when the particle moves exactly parallel to the shock normal such that  $\mu = -u$  since then, no change of position of the particle occurs in the shock rest frame. However, this is an infrequent case of particle trajectory orientation, and by decreasing the value of  $\Delta t$  sufficiently, the error becomes negligible. Therefore, the interval between two subsequent deflections is taken as  $\Delta t_d \approx 0.01$  in the downstream. The interval between two subsequent deflections in the upstream frame becomes

$$\Delta t_u = \Gamma_{rel} \Delta t_d \left(1 - \frac{\mu_d u_{rel}}{c}\right) = \Gamma_{rel} \Delta t_d (1 - \mu_d u_{rel}) \quad (15)$$

A solution of differential equation 14 is given in the form of Green's function

$$f(\mu', \phi', \Delta t) = P(\mu', \phi' | \mu'_0 = 0, \phi'_0 = 0) = \frac{1}{4\pi \Delta t} e^{-\frac{(\mu'^2 + \phi'^2)}{4\Delta t}} \quad (16)$$

Random values of  $(\mu', \phi')$  are chosen using importance sampling, related to uniformly generated random values  $(x_1, x_2)$  as:

$$\mu'(x_1, x_2) = 2\sqrt{-\Delta t \ln(1 - x_1)} \cos(2\pi x_2) \quad (17)$$

$$\phi'(x_1, x_2) = 2\sqrt{-\Delta t \ln(1 - x_1)} \sin(2\pi x_2) \quad (18)$$

New values of  $\mu$  and  $\phi$  in the original coordinate system are obtained using a rotation matrix. The initial value  $\mu_0$  (before deflection) and the final value  $\mu$  (after deflection) of the particle trajectory are related as

$$\mu = \mu_0 \cos(\phi') \sqrt{1 - \mu'^2} + \mu' \sqrt{1 - \mu_0^2} \quad (19)$$

This gives the new  $\mu$  after deflection occurs once the values of  $(\mu', \phi')$  have been randomly chosen from the PDF, given by equation 16.

The particle momentum ( $p$ ) remains unaffected by scattering events, only changing during shock crossings. The transformations of  $p$  and  $\mu$  from the upstream to downstream and vice versa are known from the Lorentz transformations (for  $c = 1$ )

$$P_u = \Gamma_{rel} P_d (1 - u_{rel} \mu_d) \quad (20)$$

$$P_d = \Gamma_{rel} P_u (1 + u_{rel} \mu_u) \quad (21)$$

$$\mu_u = \frac{\mu_d - u_{rel}}{1 - u_{rel} \mu_d} \quad (22)$$

$$\mu_d = \frac{\mu_u + u_{rel}}{1 + u_{rel} \mu_u} \quad (23)$$

In the shock rest frame this is given by

$$P_s = \Gamma_{u,d} P_{u,d} (1 + u_{u,d} \mu_{u,d}) \quad (24)$$

$$\mu_s = \frac{\mu_{u,d} + u_{u,d}}{1 + u_{u,d} \mu_{u,d}} \quad (25)$$

Additionally, to optimize computational efficiency, a boundary is established downstream, beyond which particles are unlikely to return to the shock and can be omitted from subsequent simulations. The choice of this boundary distance ( $d$ ) calculated from  $z_s = d$  such that  $f(P, \mu) = 0$  for  $\mu < -u$ , becomes

$$d = \frac{10\Gamma_d}{D_{\mu\mu}\Lambda^1} \quad (26)$$

where,  $\Lambda^1$  represents the smallest positive eigenvalue of the equation 11 (when transport equation is solved analytically).

For small  $u_d$  this can be approximated as (Kirk & Schneider 1987b)

$$\Lambda^1 \approx 6u_d\Gamma_d \quad (27)$$

However, for significant  $u_d$ , this formula underestimates  $\Lambda^1$ , potentially leading to an overestimation of  $d$ . While this overestimation doesn't increase the error, it shifts the boundary farther from the shock, reducing the probability of the particle's return.

### 3. THE MONTE-CARLO SIMULATION

To understand the simulation accurately we need to set up the Monte-Carlo simulation accordingly using several assumptions and simplification. In this section we describe the step-by-step process of our simulation model:

- The simulation starts with a set of  $N$  test particles each with four associated parameters: ( $z_s, \mu, P, w$ ) where  $w$  is the statistical weight assigned to the particle. The value of  $N$  is taken to be sufficiently large ( $\approx 10,000$ ) to ensure enough particles exist to perform DSA near the shock, and particle distribution obtained is accurately modelled (Ellison et al. 1983).
- The selection of initial values for the four parameters governs the injection scheme in the model, with a primary focus on the crucial aspect of the initial energy spectrum. We opt for a flat initial energy spectrum to observe the particle acceleration driven by DSA and its resulting energy distribution. Consequently, each particle is assigned an initial momentum value, denoted as  $P_0$  (measured in the fluid frame), set conveniently to  $P_0 = 1$ . This scales the energy axis in the energy distribution without affecting the DSA process itself. In tandem, setting the statistical weight of each particle to unity ( $w = 1$ ) ensures equal contributions to the energy distribution construction. Regarding particle positions and angular distributions, their initial values become less influential over time due to the stochastic scattering process modelled. All particles commence their journey at the shock position ( $z_s = 0$ ) and are treated as if they reside within the downstream region. Furthermore, to prevent premature particle escape, one opts for an isotropic distribution of pitch angles ( $0 \leq \mu \leq 1$ ) resembling a hemispherical velocity distribution, ensuring that all particles are directed into the downstream fluid. This enables a comprehensive analysis of various particle configurations within the simulation (Kirk & Schneider 1987a).

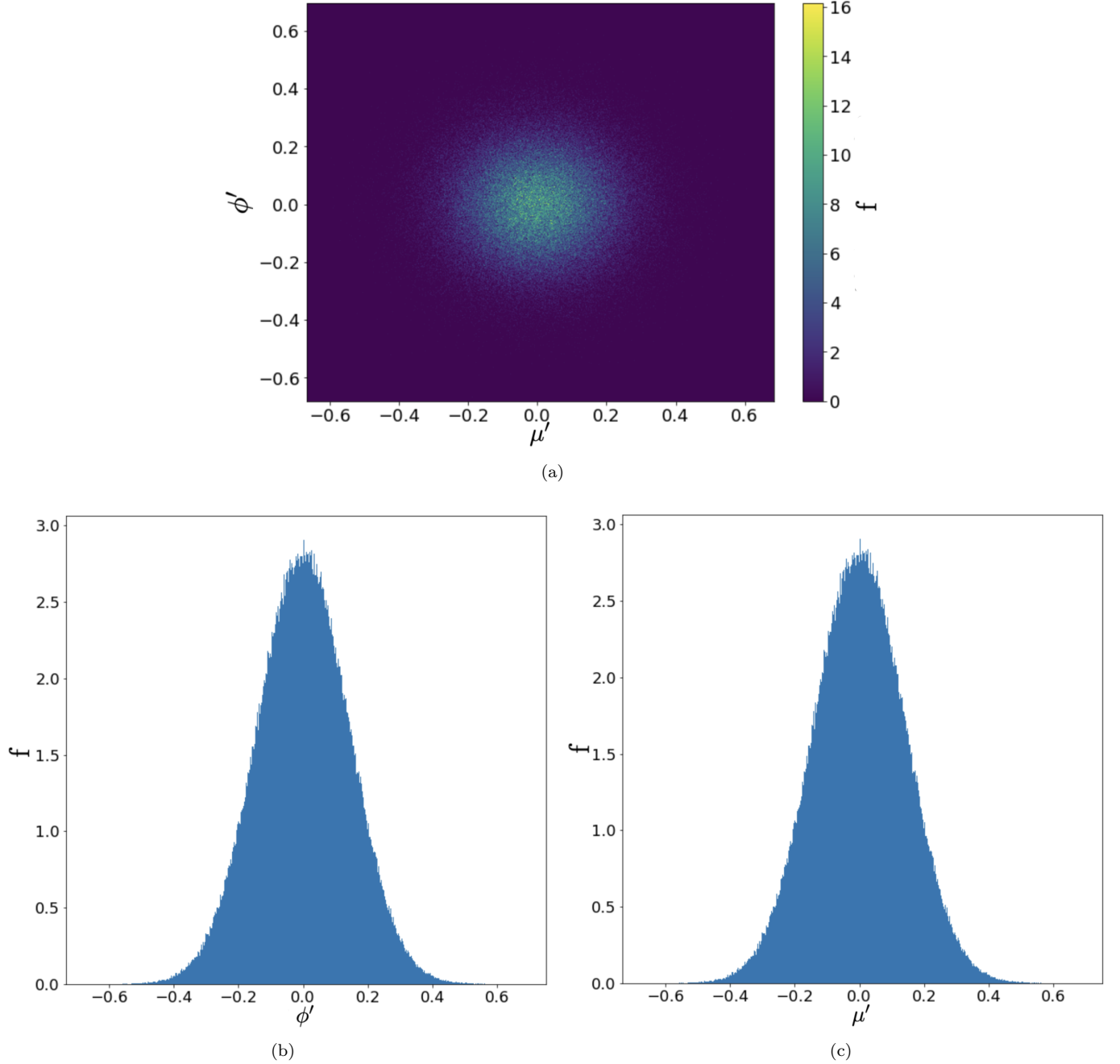


**Figure 2.** Histograms plotted to note test the distribution function ( $f$ ) of values of  $\mu'$  and  $\phi'$  obtained. (a) 2D Histogram showing distribution of  $\mu'$  and  $\phi'$  values; (b) Histogram plot of distribution of  $\phi'$  values; (c) Histogram plot of distribution of  $\mu'$  values.

- Following injection, particle propagation is governed by equation 13, wherein the parameters  $\mu$ ,  $P$ ,  $u$ , and  $\Gamma$  adapt according to the particle's position. Specifically, if a particle in the shock rest frame has a  $z$ -coordinate position  $z_s \geq 0$ , it resides within the downstream region, and its  $\mu$  and  $P$  are referenced to the downstream frame. Conversely, when  $z_s < 0$ , indicating the particle's location in the upstream region,  $\mu$  and  $P$  are measured in the upstream rest frame, with  $u = u_u$  and  $\Gamma = \Gamma_u$ . Equation 13 furnishes the change in the  $z$ -component of a particle's position in the shock rest frame, which is then added to the particle's previous  $z$ -coordinate to determine its updated  $z_s$  value. To ensure accurate particle propagation,  $\Delta t$  values differ between particles in the

downstream and upstream regions. The  $\Delta t$  value for particles in the downstream region is taken as  $\Delta t_d = 0.01$  (or smaller). Meanwhile, for particles in the upstream region, we derive  $\Delta t_u$  using equation 15 after each iteration, accounting for the changing  $\mu$  values. This ensures accurate and consistent particle evolution throughout the simulation (Kirk & Schneider 1987b).

- Consequently, a new value of  $\mu$  is determined for each particle through scattering methods. Two random numbers are generated per particle,  $(x_1, x_2)$  which are uniformly distributed in the domain  $[0, 1)$ . Utilizing these random values in equation 17 and 18, we obtain new values for  $\mu'$  and  $\phi'$  associated with each particle. These values represent the cosine of the polar and azimuthal angle in the rotated reference frame, derived from the probability density function(PDF) described in equation 16. Figure 2 shows the 2D histogram of the distribution of obtained values of  $\mu', \phi'$ . This is a test to check the values obtained using equation 17 and 18 are generating  $\mu', \phi'$  based on the 2D Gaussian PDF in 16. Additionally, the combined Gaussian PDF can be separated into two distinct Gaussian PDFs for  $\mu'$  and  $\phi'$ . Individual histograms for the distribution of values for both parameters are presented in Figure 2b and Figure 2c, demonstrating Gaussian characteristics. Subsequently, the new deflected  $\mu$  value is determined by employing the randomly generated  $\mu'$  and  $\phi'$  values, along with the previous  $\mu = \mu_0$ , as inputs in equation 19. This deflection process is consistent in both upstream and downstream fluids, as the scattering mechanisms remain identical in both regions (Kirk & Duffy 1999).
- Particle propagation continues iteratively for each particle until it crosses the shock, detected by surpassing the  $z_s = 0$  point. Upon shock crossing,  $P$  and  $\mu$  undergo Lorentz transformations to align with their corresponding values in the rest frame of the new fluid. This process mimics Fermi acceleration, where energy is also Lorentz-transformed, simulating inelastic collisions with moving Alfvén waves in the bulk fluid. If a particle moves from the upstream to downstream fluid, we apply equation 20 and equation 22; conversely, when a particle moves from downstream to upstream fluid, we use equation 21 and equation 23. It's important to note that this represents the sole mechanism for altering a particle's momentum  $P$  throughout the simulation, as scattering within their respective fluid regions does not contribute to particle acceleration. Following this, particles continue to propagate within the new fluid region, adhering to the previously outlined rules.
- The above-mentioned steps keep on repeating for every particle. Eventually, a particle crosses the boundary set at  $z_s = d$  in the downstream fluid region, given by equation 26 and equation 27, beyond which the particle stops propagating. This is modelled by checking the particle's position after each time step and noting if the value of  $z_s < d$ . As soon as the particle moves to a value of  $z_s > d$ , the particle is skipped in every future iteration and no longer propagates. The total number of simulation steps is chosen so that after finishing all iterations of particle motion, all the particles have escaped beyond the downstream boundary. This ensures no particle is still being accelerated since that could change the resultant particle energy spectrum. The aim is to observe the particle energy spectrum for all particles after their eventual escape and detection.
- In relativistic scenarios, the challenge arises from bulk motions in the shock rest frame, which can be comparable to individual particle velocities. This often results in a significant number of particles failing to overcome the bulk flow, escaping beyond the downstream boundary rather than undergoing acceleration. This high escape probability, particularly at higher momentum values, can lead to a loss of statistical accuracy, given a fixed initial number of particles. While an actual plasma contains an infinite pool of particles for acceleration, simulations must define particle limits in advance. Selecting an excessive number of particles can be computationally impractical.

To address this, the "particle splitting" mechanism is introduced. A predefined splitting factor denoted as  $N_d$ , indicates the number of daughter particles a single particle splits into. When a particle crosses from downstream to upstream, it divides into  $N_d$  daughter particles. These daughters inherit the original particle's  $z_s$ ,  $P$ , and  $\mu$  values, but with a statistical weight of  $w = \frac{1}{N_d}$ . Each of these daughters then follows the propagation rules outlined earlier, resulting in distinct trajectories due to stochastic scattering. This approach ensures that particles returning to the shock for further acceleration maintain sufficient representation for statistical accuracy. To prevent an excessive proliferation of daughter particles with negligible contributions to the energy spectrum, a lower limit on statistical weight is defined. This limit is determined by considering the maximum momentum value of interest in the spectrum and ensuring the accurate representation of a power-law distribution.  $N_d$  is defined as  $N_d = \frac{P_{esc}}{1 - P_{esc}}$ , where  $P_{esc}$  represents the probability of particle escape. Estimating  $P_{esc}$  for the system

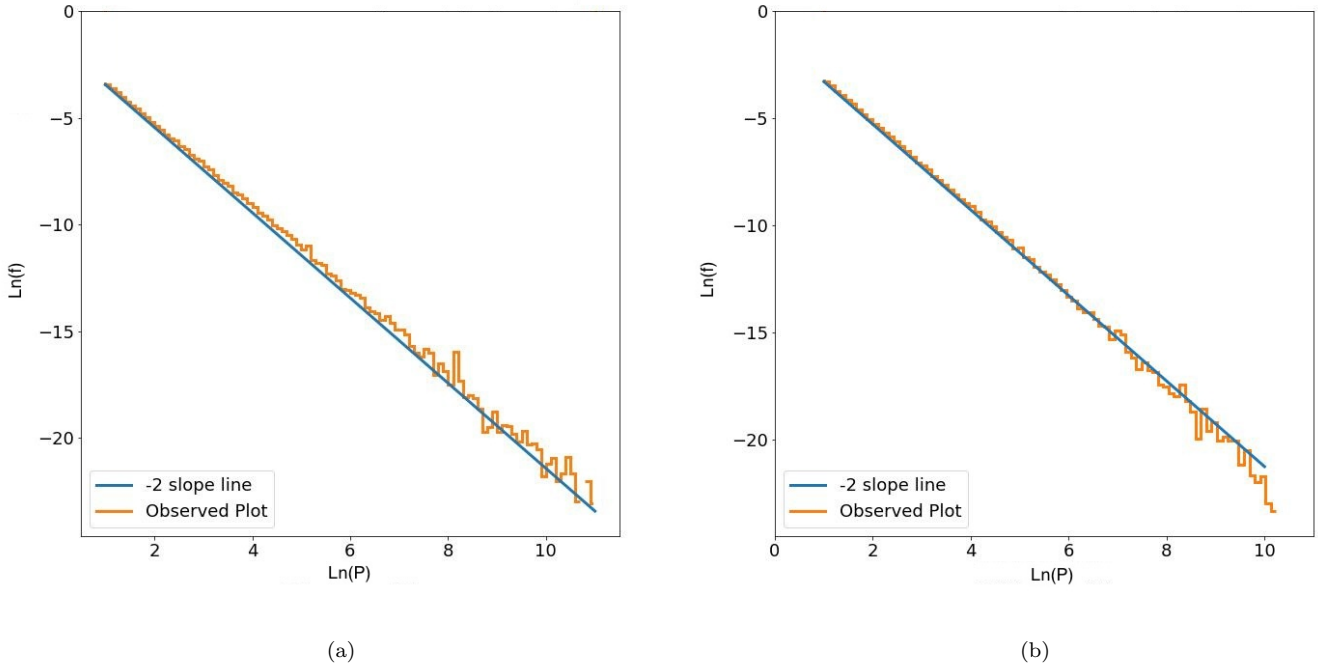


**Figure 3.** Plots illustrate Power-law energy spectra for non-relativistic shock using DSA simulations. In figure (a)  $u_u = \frac{c}{2}$  and  $u_d = \frac{c}{8}$ , and figure (b), with  $u_u = \frac{c}{4}$  and  $u_d = \frac{c}{16}$ , considering a constant diffusion coefficient. Plots are showing the slope  $\sim 2$ , which is consistent with existing simulations as well as theory results.

enables the maintenance of a relatively constant average number of simulated particles, particularly at higher momentum values.

- Prior, a distribution function is established, organized into momentum bins of equal length, initially set to zero for each bin. Whenever a particle crosses the shock, its momentum ( $P$ ) and cosine of the pitch-angle ( $\mu$ ) are recorded and transformed to the shock rest frame using equation 24 and 25 for measurement. The distribution function updates based on the particle's momentum in the shock rest frame, incrementing the corresponding bin's value by  $\frac{w}{|\mu_s|}$ . The inclusion of  $\frac{1}{|\mu_s|}$  alongside statistical weight ensures that the distribution function reflects the particle flux across the shock rather than the energy spectrum. This factor mitigates the dominance of particles with higher  $|\mu_s|$  values, which are more likely to cross the shock and would disproportionately influence the spectrum. This process continues throughout the simulation until its conclusion. The distribution function values are then plotted against the corresponding momentum bins to obtain the particle energy spectrum. Given the expected power law, it is often more useful to plot the natural logarithm of the distribution function (representing particle number density) against the natural logarithm of momentum bin values. The slope of the resulting curve allows the determination of the spectral index  $s$  through the least-squares fitting method, providing insight into the observed power-law spectrum (Frenkel & Smit 2001).

#### 4. RESULTS

Following the methodology outlined above, the simulation code is solved to determine the spectral index in non-relativistic and special relativistic scenarios. A power-law momentum distribution is observed by employing a suitable number of particles, typically  $N = 10,000$ , and an appropriate number of simulation steps. Using the least-squares fitting method, the slope of the plot, which represents the natural logarithm of the distribution function  $f$  against the natural logarithm of momentum  $P$  (representing energy), is calculated. This slope corresponds to  $-s$ , where  $s$  denotes the spectral index characterizing the power-law energy distribution. The input to the simulation code is the bulk velocity  $u_u$  and  $u_d$  measured in the shock rest frame, determining the type of shock under consideration. We



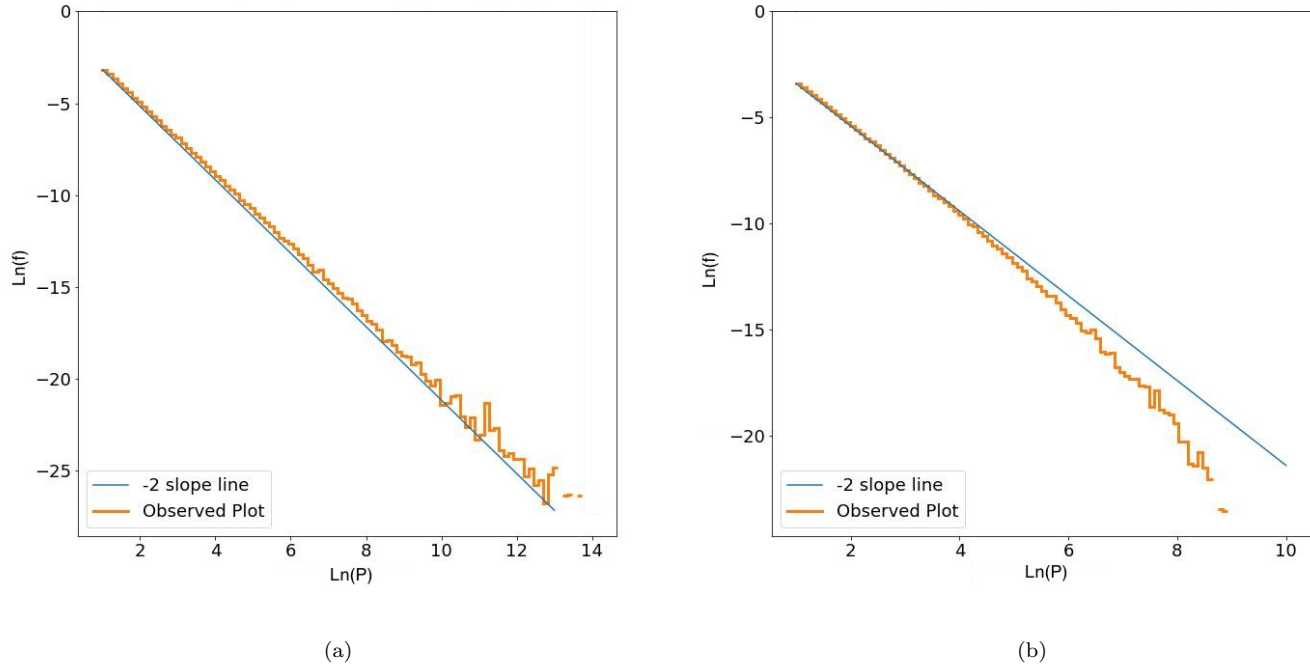


**Figure 4.** Plots showing Power-law energy spectra for momentum( $P$ ) dependent diffusion co-efficient in non-relativistic shocks. In figure (a), the shock velocities are  $u_u = \frac{c}{2}$  and  $u_d = \frac{c}{8}$ , while in figure (b), the velocities are  $u_u = \frac{c}{4}$  and  $u_d = \frac{c}{16}$ . The observed plots from the simulation deviate from the theoretically expected slope of  $\sim 2$ , known from theory, indicating that low-momentum particles diffuse more easily than high-momentum particles.

have used an ultra-relativistic equation of state, which is often applied to scenarios involving highly energetic particles moving at speeds close to the speed of light.

In our simulations, we explored various forms of the diffusion coefficient,  $D_{\mu\mu}(P)$ , depending on the power spectrum of magnetic fluctuations. In scenarios following quasi-linear theory, where the power spectrum is inversely proportional to the wavenumber  $k$ ,  $D_{\mu\mu}$  is considered independent of  $\mu$ . In the absence of radiation losses, it also remains independent of momentum, taking the form  $D_{\mu\mu}(P) = D_0$  (Kirk & Schneider 1987a). However, when the power spectrum follows a Kolmogorov spectrum,  $D_{\mu\mu}$  becomes proportional to  $\mu$  (Kirk 2005). In the absence of radiation losses, we adopt the form  $D_{\mu\mu} = D_0(1 - \mu^2)$  to account for this dependence on pitch angle (Kirk & Duffy 1999). Moreover, considering the Fokker-Planck type transport equation, the momentum dependence of the diffusion coefficient significantly influences the spatial distribution of particles near shocks. For simplicity, we assume a power-law dependence on momentum, specifically  $D_{\mu\mu} = D_0 P^{-1}$ , where  $D_0$  represents the isotropic diffusion co-efficient (Kirk & Schneider 1987b).

#### 4.1. Spectral Index in Non-Relativistic Case

Assuming the isotropic diffusion with no radiation losses, the pitch-angle diffusion co-efficient ( $D_{\mu\mu}(P)$ ) is assumed to be independent of  $\mu$  and  $P$ , i.e.,  $D_{\mu\mu} = D_0$ . The spectral index for non-relativistic shocks depends only on the compression ratio. Considering a non-relativistic strong shock with mono-atomic ambient fluid, the relation between upstream and downstream fluid velocities is  $\frac{u_u}{u_d} \approx 4$ . Assuming  $u_u$  to be  $c/2$  or  $c/8$  and corresponding  $u_d$  to be  $c/8$  or  $c/16$ ,  $s$  comes out to be  $\sim 2$ , which is close to analytically calculated value,  $s_a = 2$  (as shown in figure 3) (Longair 2011).

Assuming the diffusion coefficient to vary as  $D_{\mu\mu} = D_0 P^{-1}$ , figure 4 shows how the spectral index changes when the diffusion coefficient is a function of momentum. The deviation of the spectral index from its usual value ( $-2$ ) becomes larger as the fluid velocity becomes smaller (although the compression ratio remains the same). Figure 5 shows the deviation of the spectral index (from  $-2$ ) when the diffusion co-efficient varies with  $\mu$  ( $D_{\mu\mu} = D_0(1 - \mu^2)$ ). The change in the spectral index is quite significant for this case. For lower fluid velocities (in both the upstream

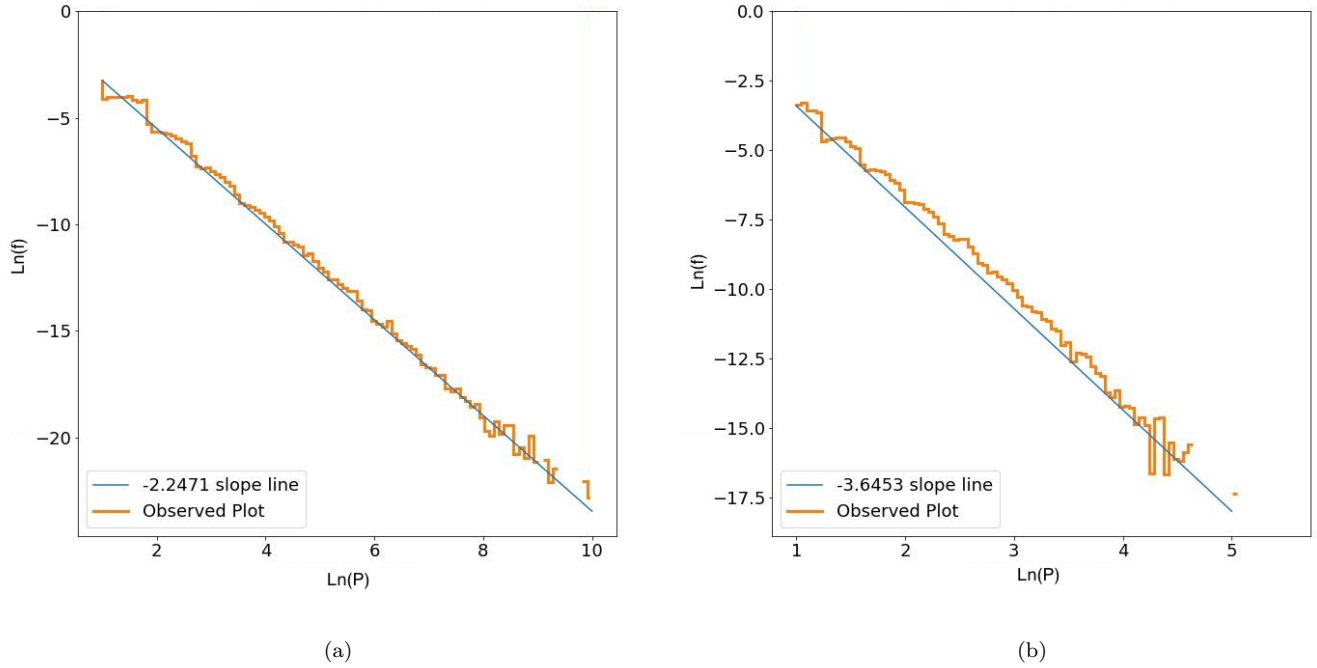


**Figure 5.** Plots depict Power-law energy spectra for non-relativistic cases with a pitch angle( $\mu$ ) dependent diffusion coefficient. Figure (a) shows results for high upstream velocity ( $u_u = \frac{c}{2}$  and  $u_d = \frac{c}{8}$ ), displaying an observed slope of approximately 2. Despite a slight oscillatory nature due to quadratic pitch angle dependence, the plot aligns with the expected slope. Figure (b) illustrates a case with lower upstream velocity ( $u_u = \frac{c}{4}$  and  $u_d = \frac{c}{16}$ ), deviating significantly from the expected slope of approximately 2. The deviation is attributed to the quadratic dependence on pitch angle, highlighting the impact of velocity variations on the energy spectrum.

and downstream), the spectral index takes larger values (compared to the momentum dependence of the diffusion coefficient).

#### 4.2. Spectral Index in Relativistic Case

Beyond the cases discussed above, little information is available on the shocks involving DSA in real astrophysical scenarios. The EoS for the upstream and downstream regions and the velocity relationships between the bulk fluid regions need to be better known for realistic astrophysical scenarios.

Assuming the EoS are the same for both the upstream and downstream regions, we assume it of the form (Rezzolla & Zanotti 2013)

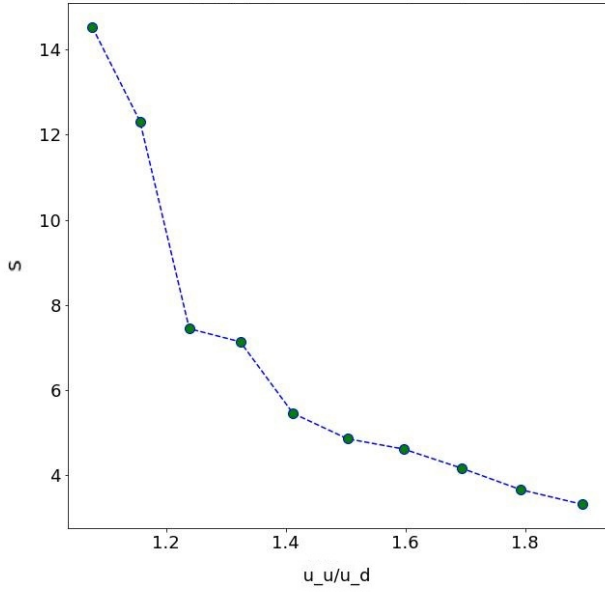
$$p = \frac{\epsilon}{n} \quad (28)$$

where the value  $n$  can be varied, and depending upon  $n$ , one gets mildly-relativistic EoS to ultra-relativistic EoS. In the equation,  $p$  represents the pressure of the fluid in question and  $\epsilon$  is the internal energy per unit mass. It is a generalized form of the equation  $p = (\gamma - 1)(e - \rho)$ , a gas whose pressure is dominated by a relativistic component (implies  $e \gg \rho$ ), where  $\gamma$  can be identified as the ratio of specific heats of the gas. For this EoS, the relation between the velocities becomes (from equation 8)

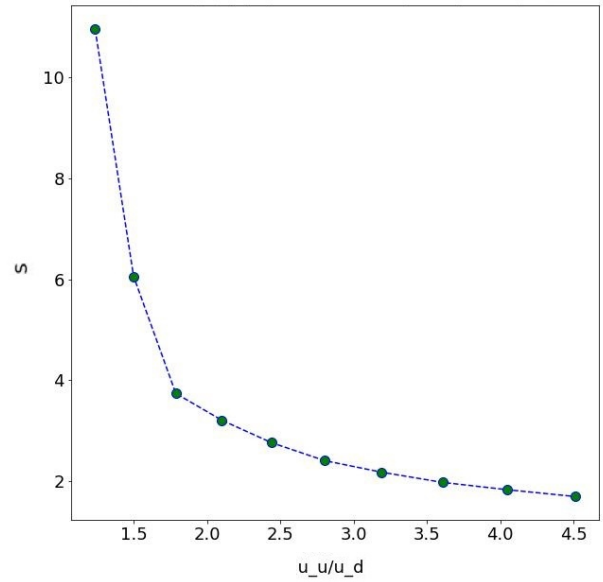
$$u_u u_d = \frac{c^2}{n} \quad (29)$$

For shocks ( $u_u > u_d$ ), the values of  $u_u$  and  $u_d$  must obey  $0 < u_d < u_u < c$ . Using Equation 29, this can be represented as

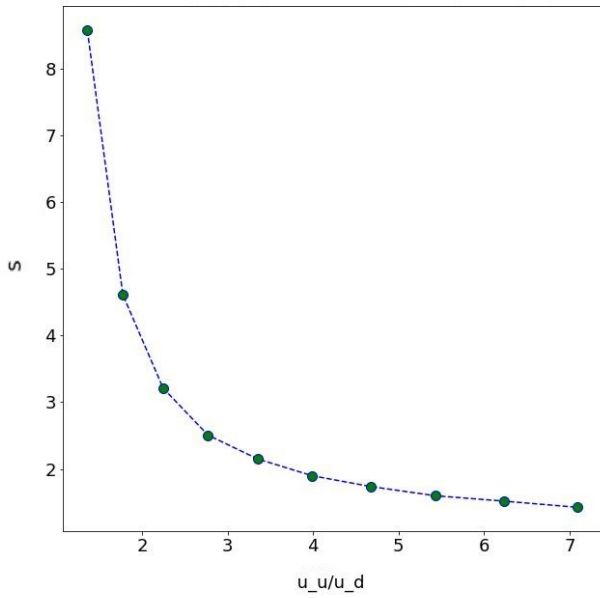
$$\frac{c^2}{nu_u} < u_u < c$$



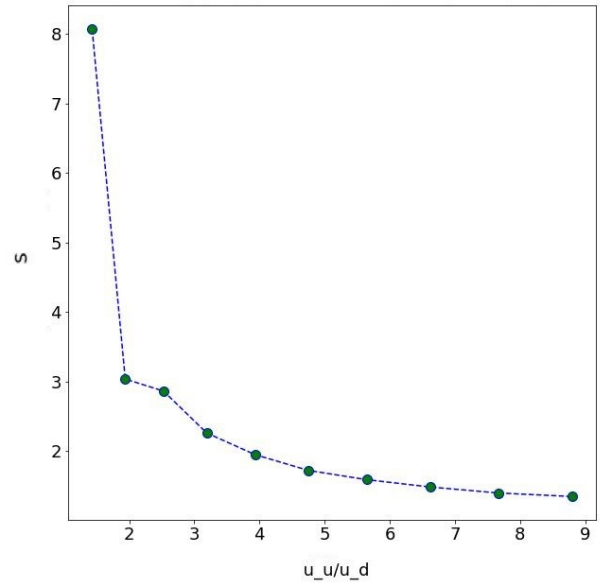
(a)



(b)

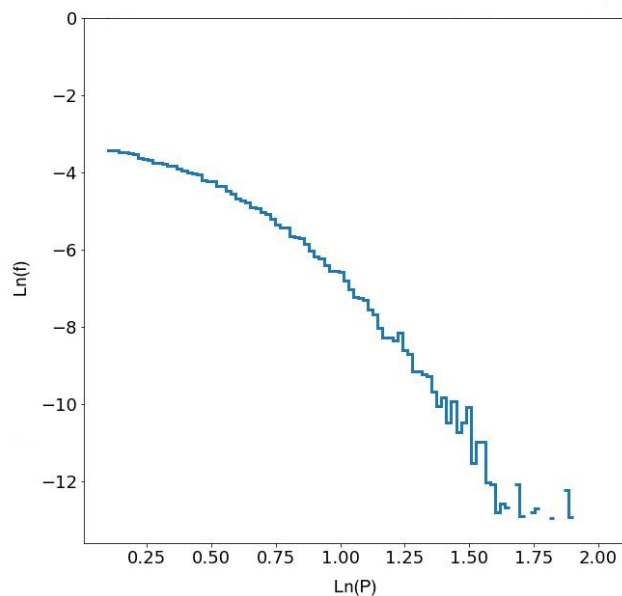


(c)

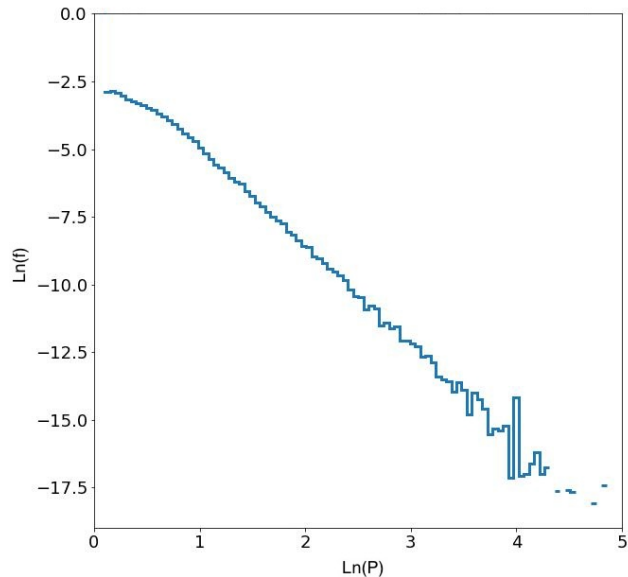


(d)

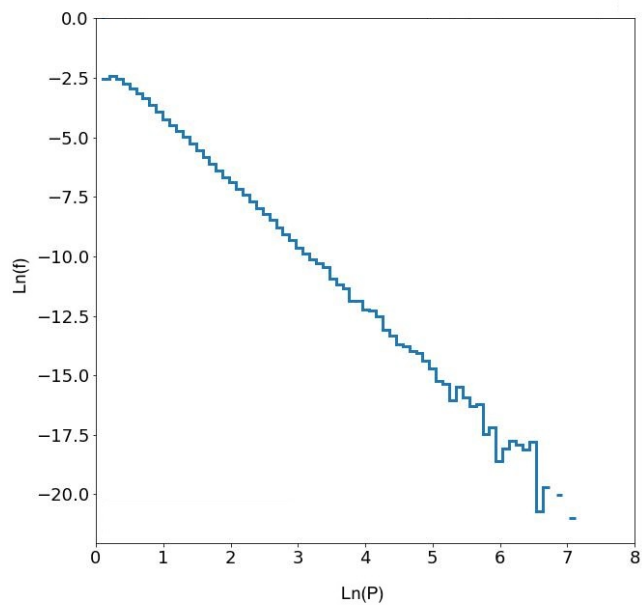
**Figure 6.** The plots displayed in the figures are  $s$  vs  $\frac{u_u}{u_d}$  (compression ratio) with constant diffusion co-efficient. The trend observed is similar for all EOS considered, with a decreasing value of  $s$  as the velocity ratio value  $\frac{u_u}{u_d}$  increases. In almost all cases of EOS considered, the velocity ratio  $\frac{u_u}{u_d}$  corresponding to observed values of  $s$  are in the range  $\approx 2 - 3$ . Therefore, in the normal shock case, a velocity ratio range corresponding to the experimentally observed power-law spectral distribution is estimated for multiple ambient fluid EOS considered.



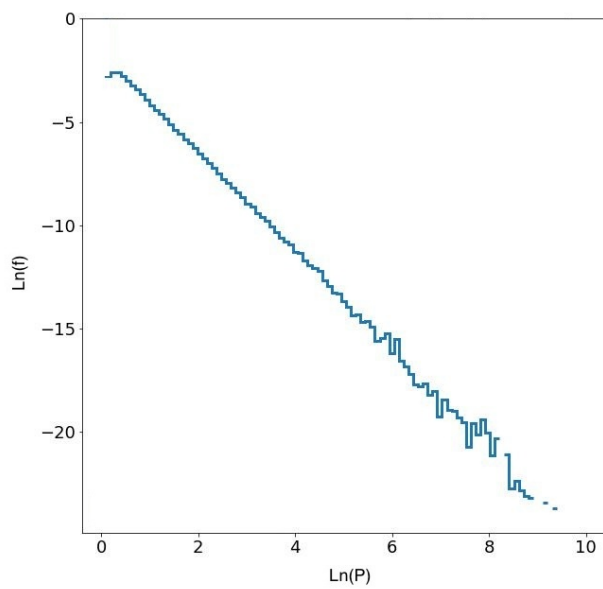
(a)



(b)



(c)



(d)

**Figure 7.** The plots displayed in the figures are  $\ln(f)$  vs.  $\ln(P)$  with momentum dependent diffusion co-efficient. The observed trend is consistent across all considered EOS, showing a decrease in the number of particles as momentum increases. This behavior can also be analyzed using the diffusion co-efficient. As depicted in the plot, particles with higher momentum exhibit lower diffusivity, indicating that they diffuse in fewer numbers compared to particles with lower momentum. Consequently, in the case of an arbitrarily strong shock, calculating the slope directly is not feasible due to the non-linearity of the plots.

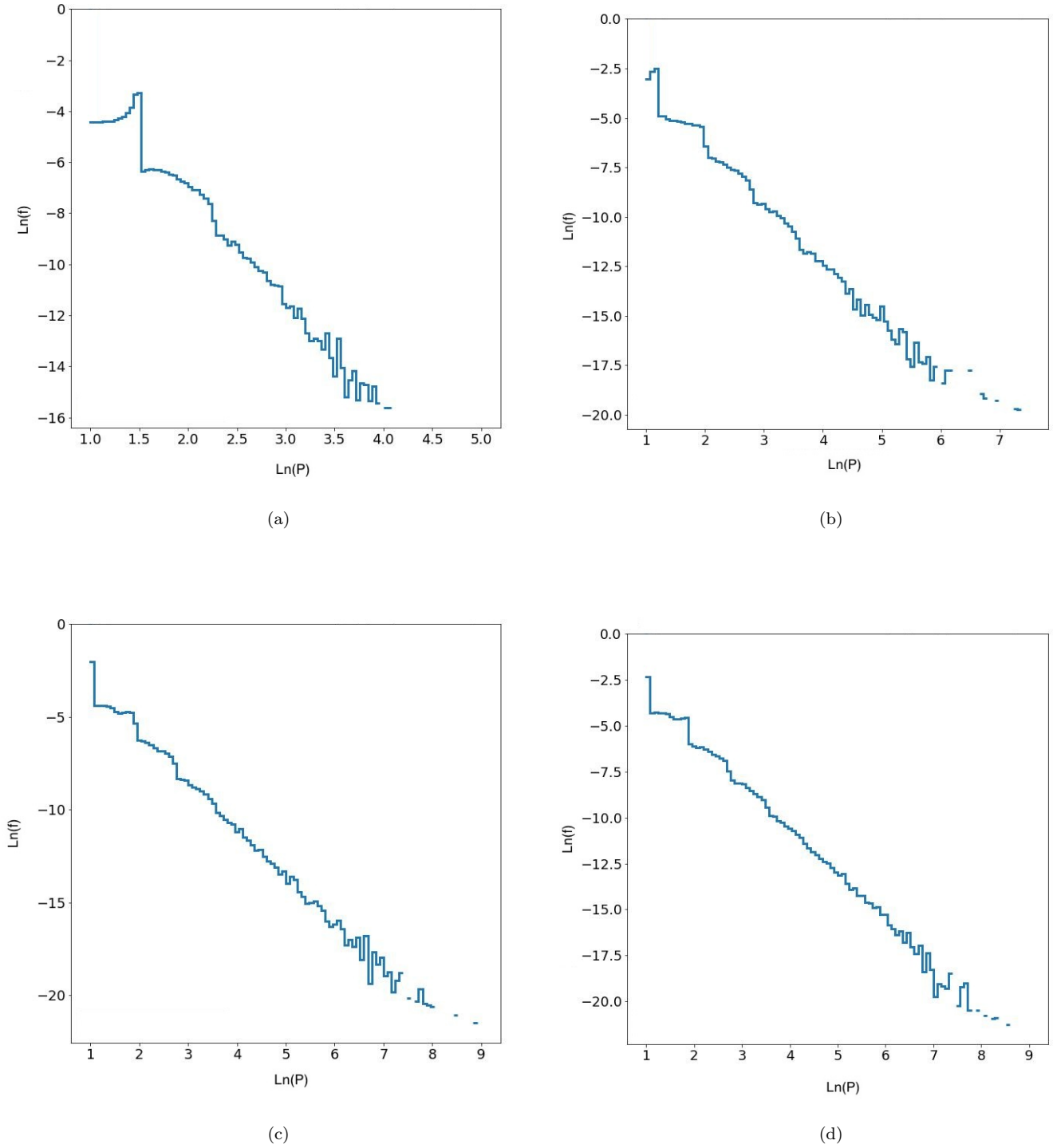


**Figure 8.** The plots displayed in the figures are  $\text{Ln}(f)$  vs.  $\text{Ln}(P)$  with pitch angle dependent diffusion co-efficient. The sinusoidal behavior observed in each plot reflects the pitch angle dependence of the diffusion co-efficient ( $\sim \text{Sin}^2(\theta)$ ). In this case as well, calculating the slope is not feasible due to the non-linearity of the plots.

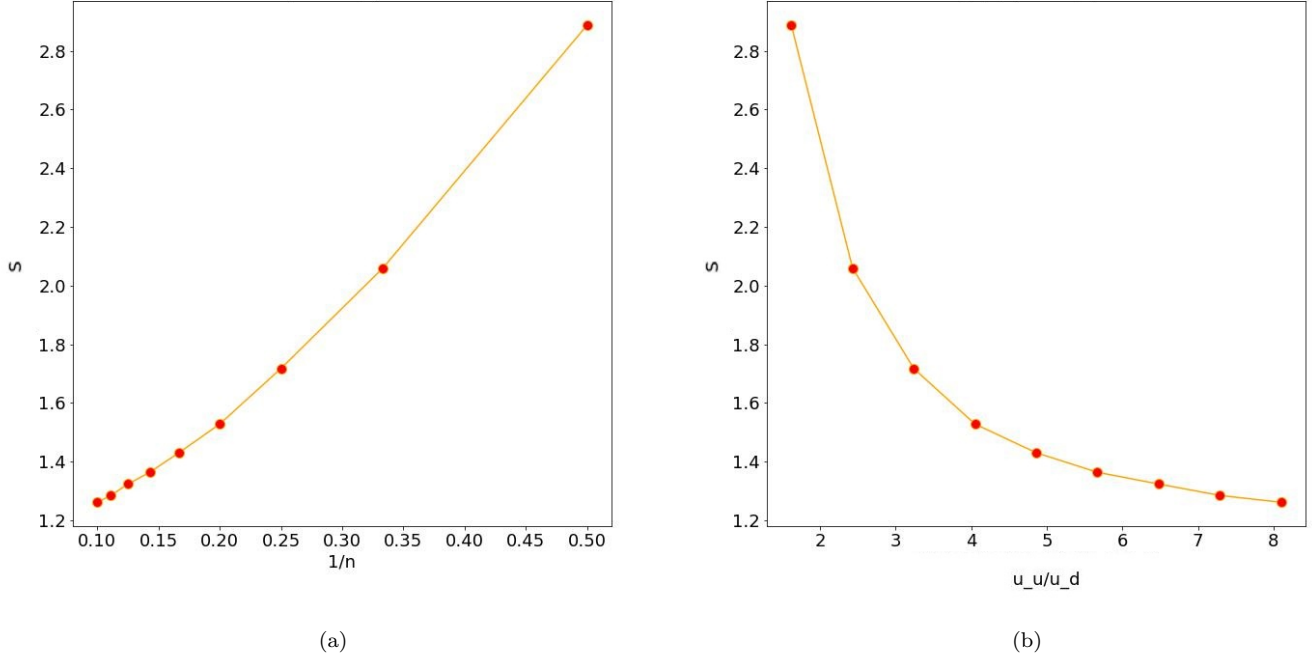


**Figure 9.** The spectral index ( $s$ ) values are plotted with respect to  $\frac{1}{n}$  and bulk velocity ratio ( $\frac{u_u}{u_d}$ ) to observe the dependence of spectral index on equations of state in a strong ultra-relativistic ( $u_u = 0.99c$ ) shock case with constant diffusion co-efficient. The plot is shown in Figure (a). An almost linear relationship is observed between  $s$  and  $\frac{1}{n}$  for high  $n$  values in the strong shock case, with slight deviation for smaller  $n$  values as the slope becomes steeper. One already notes the direct correspondence between  $u_d$  and  $n$  values from Equation 29; therefore, no new information can be derived from a plot between  $s$  and  $u_d$ . However,  $s$  is also plotted with respect to velocity ratio  $\frac{u_u}{u_d}$  to note the velocity ratio values in strong shocks that give the spectral index  $s$  in the observed range  $\approx 2 - 3$ . The plot is shown in Figure (b). Note from the figure that the values of bulk velocity ratio  $\frac{u_u}{u_d}$  lying in the range  $\approx 1.5 - 2.5$  give  $s$  in the range  $\approx 2 - 3$  for strong shock case. Therefore, for strong astrophysical shocks that may produce the observed cosmic ray particles, the bulk velocity ratio is estimated to be in the range  $\approx 1.5 - 2.5$ .

or more simply

$$u_u^2 > \frac{c^2}{n} \implies u_u > \frac{c}{\sqrt{n}}$$

. Therefore, for some chosen value of  $n$ , the possible values of upstream bulk velocities satisfy

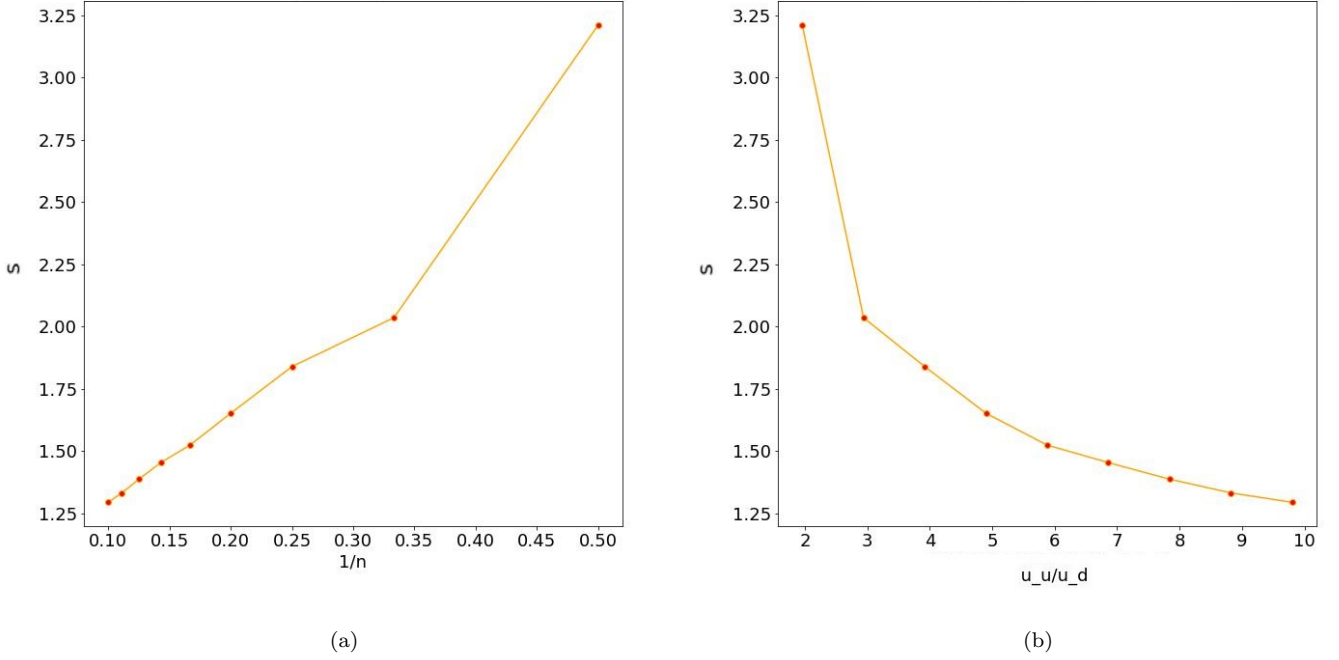
$$\frac{c}{\sqrt{n}} < u_u < c \quad (30)$$

We can then categorize two cases depending on the value of  $u_u$ . A normal shock can be generated if  $u_u < c$ ; however, we have a strong shock if  $u_u \approx c$ .

#### 4.3. $u_u < c$

For  $u_u < c$ , one can vary  $n = 2, 5, 8, 10$ . A higher value of  $n$  almost makes the EoS non-relativistic and does not generate any new physics. While  $p = \epsilon$  represents the causality limit of the EoS ( $n = 1$ ). For this EoS, one can simulate DSA for three different diffusion coefficients.

Figure 6 shows  $s$  as a function of compression ratio for  $D_{\mu\mu} = D_0$ . The spectral index decreases as the compression ratio increases, a trend consistent across all  $n$  values. Additionally, Figures 6 indicate that for  $s$  to fall within the observed range ( $\sim 2 - 3$ ), the compression ratio should be greater than 1.8 for  $n = 2$ , lie between 2.5 to 3.5 for  $n = 5$ , and roughly between 2.2 to 3.5 for  $n = 8$ , and between 2.2 to 4 for  $n = 10$ . This suggests that as EoS becomes softer, the spectral index consistently falls within the range observed in cosmic ray spectra for a broad span of compression ratio values.



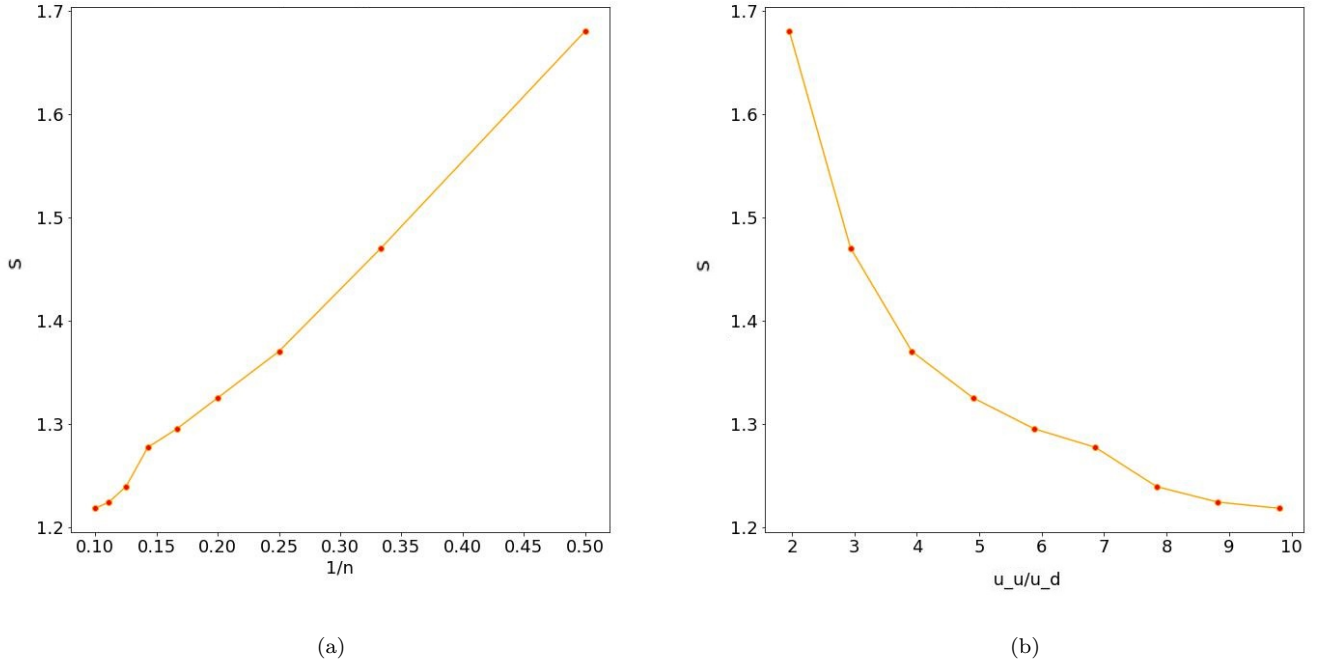
**Figure 10.** The spectral index ( $s$ ) values are plotted with respect to  $\frac{1}{n}$  and bulk velocity ratio ( $\frac{u_u}{u_d}$ ) to observe the dependence of spectral index on equations of state in a strong ultra-relativistic ( $u_u = 0.99c$ ) shock case with diffusion co-efficient dependent on momentum ( $P$ ). The plot shown in Figure (a) illustrates the spectral index values between 2 and 3, which represent the slope of observed cosmic rays. These values are calculated for a range of  $n$  from 2.2 to 3.2, corresponding to bulk velocity ratio values ranging from 2.2 to 3. It can be inferred that in the case of a strong shock, where velocities are very high, the momentum dependence of the diffusion co-efficient has minimal impact on the cosmic ray spectrum and show similar result as for constant diffusion co-efficient. Consequently, the results are similar to those obtained when assuming a constant diffusion co-efficient.

Figure 7 shows results when the diffusion coefficient varies with momentum as  $D_{\mu\mu} = D_0 P^{-1}$ . The plots illustrate that the particles with higher momentum diffuse in smaller quantities compared to those with lower momentum. Additionally, with increasing momentum, the slope of the curve changes, causing a shift in the spectral index. This shift leads to a non-linear spectrum, making it challenging to determine a specific value for the spectral index. However, as EoS becomes softer, a more linear spectrum is obtained (spectral index can be estimated). In Figure 7a, the spectrum is entirely non-linear, making it challenging to determine a specific value of the spectral index. For  $n = 5$  in Figure 7b,  $s$  can be estimated to be around 3.5, and similarly for  $n = 8$  in figure 7c the spectral index is approximately 3.0. For  $n = 10$  in Figure 7d, the spectral index comes out to be around 2.2.

Finally, when the diffusion co-efficient depends on  $\mu$  ( $D_{\mu\mu} = D_0 (1 - \mu^2)$ ) we obtain the particle spectrum, depicted in figure 8, reveals a changing slope with momentum. At lower momentum values, the slope of the curve initially shows a sinusoidal pattern, creating ambiguity in defining the spectral index (revealing a dependency of the diffusion coefficient on pitch angle). However, with an increase in the  $n$  value in the EoS, the sinusoidal behaviour diminishes, suggesting a reduced influence of the diffusion coefficient on the spectrum. Determining the spectral index for ( $n = 2$ ) is difficult, but as  $n$  increases, we can have a rough estimate of the spectral index. For  $n = 5$   $s$  is equal to 3.4 for  $n = 8$   $s$  is 2.7 and for  $n = 10$   $s$  is 2.3.

#### 4.4. $u_u \approx c$

When the velocity of the upstream particles approaches the speed of light, we have ultra-relativistic shocks (in our case  $u_u = 0.99c$ ). By considering different values for  $n$  with  $u_u = 0.99c$ , we determined the downstream velocity ( $u_d$ ) using equation 29. The simulations were performed for 9 cases, and we analyzed the spectral index values obtained from the power-law spectral energy distribution as shown in figures 9, 10, and 11.



**Figure 11.** The spectral index ( $s$ ) values are plotted with respect to  $\frac{1}{n}$  and bulk velocity ratio ( $\frac{u_u}{u_d}$ ) to observe the dependence of spectral index on equations of state in a strong ultra-relativistic ( $u_u = 0.99c$ ) shock case with diffusion co-efficient dependent on  $1 - \mu^2$ . The plots clearly demonstrate that it is not possible to obtain an observed spectral index of cosmic rays' spectrum using a diffusion co-efficient that depends on pitch angle with strong shocks. This is because when such a diffusion co-efficient is applied with strong shock, the higher velocity particles tend to exhibit a less steep slope in the spectrum. In practical terms, this means that low-momentum particles diffuse more readily than their high-momentum counterparts, and vice versa.

Interestingly, regardless of whether the diffusion coefficient is constant or depends on parameters like momentum ( $P$ ) or pitch angle ( $\mu$ ), we consistently observed a linear spectrum in each case. However, the range of spectral indices varied for each scenario. With a constant diffusion coefficient, the slope ranged between 1.2 to 2.9, covering the observed cosmic ray spectrum. Similarly, when the diffusion coefficient depends on momentum, the slope varied from 1.25 to 3.25, still encompassing the observed cosmic ray spectra. However, when we looked at the slope range for a pitch angle-dependent diffusion coefficient, it only ranged from 1.2 to 1.7, implying that one cannot replicate the observed cosmic ray spectrum for ultra-relativistic shocks using such EoS.

## 5. SUMMARY AND DISCUSSION

This study focuses on numerically modelling the Diffusive Shock Acceleration (DSA) of cosmic ray particles using a Monte Carlo simulation based on the Kirk and Schneider model (Kirk & Schneider 1987b). The primary goal is to simulate DSA in both non-relativistic and relativistic scenarios. The code underwent rigorous testing, examining three DSA cases previously analyzed theoretically by Kirk and Ballard (using an eigenfunction method) (Kirk & Schneider 1987a; Ballard & Heavens 1991). In non-relativistic shock scenarios, we explored various diffusion coefficients, finding that the spectral index varies with diffusion coefficients, particularly when influenced by momentum or pitch angle. In the relativistic cases, both normal shock and ultra-relativistic shocks ( $u_u = 0.99c$ ) were investigated, utilizing relativistic EoSs (Landau & Lifshitz 1987; Rezzolla & Zanotti 2013).

For non-relativistic shocks, we established that the spectral index relies on the compression ratio, exhibiting variations with different diffusion coefficients influenced by momentum or pitch angle. In relativistic normal shock with constant diffusion co-efficient, as EoS becomes softer, the range for compression ratio for which one obtains a spectral index close to that found observationally increases. However, when the diffusion coefficient varies with momentum or pitch angle, it is difficult to determine the spectral index for stiffer EoS as the spectrum becomes highly non-linear. However,



as the EoS becomes softer, the spectrum starts to become more and more linear, and one can have an estimate of the spectral index. As the EoS becomes softer, the spectral index decreases and stays around the observational limit.

Surprisingly, in ultra-relativistic scenarios, we consistently observed a linear spectrum, irrespective of the diffusion coefficient type (constant, momentum-dependent, or pitch angle-dependent). However, the range of spectral indices varied for each case. At the same time, constant and momentum-dependent diffusion coefficients aligned with the observed cosmic ray spectrum, but pitch angle-dependent coefficients did not, highlighting limitations in certain equations of state. These findings provide valuable insights into the complex dynamics of shock acceleration in different astrophysical scenarios.

The Monte Carlo simulation code, created to model DSA for both fast and slow shocks with specific diffusion features, has wide applications in astrophysics. With the inclusion of relativistic EoS, we achieved more accurate estimates of the ambient fluid's properties. This improvement can assist in identifying the types of shocks present in energetic astrophysical phenomena that produce observed cosmic ray spectra. Currently, the diffusion equation assumes no non-linear dependence on the distribution function. However, future considerations may involve a more realistic diffusion equation with non-linear terms, especially considering the effects of stochastic scattering due to Alfvén waves influenced by the distribution function of particles. A crucial aspect for future enhancements is the potential inclusion of a general relativistic formulation (Mallick & Verma 2022; Verma & Mallick 2023), accounting for gravitational influences. Adapting the simulation model for general relativistic scenarios in high-energy astrophysical phenomena could lead to power-law energy spectra more closely aligned with experimental observations. These modifications would optimize the DSA simulation, offering valuable insights into the structure and properties of high-energy astrophysical sources responsible for particle acceleration.

#### ACKNOWLEDGEMENTS

The authors would like to thank the Indian Institute of Science Education and Research Bhopal for providing all the research and infrastructure facilities. AV would like to acknowledge the Prime Minister's Research Fellowship (PMRF), Ministry of Education Govt. of India, for a graduate fellowship and RM acknowledges Science and Engineering Research Board (SERB), Govt. of India, for monetary support in the form of Core Research Grant (CRG/2022/000663).

#### REFERENCES

- Aartsen, M. G., Abbasi, R., Abdou, Y., et al. 2013, *Phys. Rev. D*, 88, 042004, doi: [10.1103/PhysRevD.88.042004](https://doi.org/10.1103/PhysRevD.88.042004)
- Abeyssekara, A., Alfaro, R., Alvarez, C., et al. 2019, *ApJ*, 871, 96, doi: [10.3847/1538-4357/aaf5cc](https://doi.org/10.3847/1538-4357/aaf5cc)
- Acerro, F., Ackermann, M., Ajello, M., et al. 2015, *The Astrophysical Journal Supplement Series*, 218, 23
- Achterberg, A., Blandford, R. D., & Reynolds, S. P. 1994, *A & A*, 281, 220
- Achterberg, A., Gallant, Y. A., Kirk, J. G., & Guthmann, A. W. 2001a, *Monthly Notices of the Royal Astronomical Society*, 328, 393, doi: [10.1046/j.1365-8711.2001.04851.x](https://doi.org/10.1046/j.1365-8711.2001.04851.x)
- . 2001b, *Monthly Notices of the Royal Astronomical Society*, 328, 393, doi: [10.1046/j.1365-8711.2001.04851.x](https://doi.org/10.1046/j.1365-8711.2001.04851.x)
- Adriani, O., Barbarino, G. C., Bazilevskaya, G. A., et al. 2014, *ApJ*, 791, 93, doi: [10.1088/0004-637X/791/2/93](https://doi.org/10.1088/0004-637X/791/2/93)
- Aguilar, M., Aisa, D., Alpat, B., et al. 2015, *PhRvL*, 115, 211101, doi: [10.1103/PhysRevLett.115.211101](https://doi.org/10.1103/PhysRevLett.115.211101)
- Alfvén, H. 1943, *Arkiv for Matematik, Astronomi och Fysik*, 29B, 1
- Allen, M. P., & Tildesley, D. J. 1989, *Computer Simulation of Liquids* (Oxford: Clarendon Press)
- Apel, W., Arteaga-Velázquez, J., Bekk, K., et al. 2014, *Advances in Space Research*, 53, 1456, doi: <https://doi.org/10.1016/j.asr.2013.05.008>
- Arzner, K., Knaepen, B., Carati, D., Denewet, N., & Vlahos, L. 2006, *ApJ*, 637, 322, doi: [10.1086/498341](https://doi.org/10.1086/498341)
- Arzner, K., & Vlahos, L. 2004, *ApJL*, 605, L69, doi: [10.1086/392506](https://doi.org/10.1086/392506)
- Axford, W. I., Leer, E., & Skadron, G. 1977, in *International Cosmic Ray Conference*, Vol. 11, *International Cosmic Ray Conference*, 132
- Ballard, K. R., & Heavens, A. F. 1991, *Monthly Notices of the Royal Astronomical Society*, 251, 438, doi: [10.1093/mnras/251.3.438](https://doi.org/10.1093/mnras/251.3.438)
- Bell, A. R. 1978, *Monthly Notices of the Royal Astronomical Society*, 182, 147, doi: [10.1093/mnras/182.2.147](https://doi.org/10.1093/mnras/182.2.147)
- . 2004, *Monthly Notices of the Royal Astronomical Society*, 353, 550, doi: [10.1111/j.1365-2966.2004.08097.x](https://doi.org/10.1111/j.1365-2966.2004.08097.x)
- Berezhko, E. G., Ksenofontov, L. T., & Völk, H. J. 2002, *A&A*, 395, 943, doi: [10.1051/0004-6361:20021219](https://doi.org/10.1051/0004-6361:20021219)
- Biermann, P. L., Kronberg, P. P., Allen, M. L., Meli, A., & Seo, E.-S. 2019, *Galaxies*, 7, doi: [10.3390/galaxies7020048](https://doi.org/10.3390/galaxies7020048)

- Blandford, R., & Eichler, D. 1987, *Physics Reports*, 154, 1, doi: [https://doi.org/10.1016/0370-1573\(87\)90134-7](https://doi.org/10.1016/0370-1573(87)90134-7)
- Blandford, R., & Ostriker, J. 1978, *The Astrophysical Journal Letters*, 221, L29, doi: [10.1086/182658](https://doi.org/10.1086/182658)
- Csernai, L. P. 1994, *Introduction to relativistic heavy ion collisions* (John Wiley & Sons Ltd). <http://www.csernai.no/Csernai-textbook.pdf>
- Drury, L. O. 1983, *Reports on Progress in Physics*, 46, 973, doi: [10.1088/0034-4885/46/8/002](https://doi.org/10.1088/0034-4885/46/8/002)
- Ellison, D. C., Jones, F. C., & Eichler, D. 1983, in *International Cosmic Ray Conference*, Vol. 2, *International Cosmic Ray Conference*, 271
- Fermi, E. 1949, *Phys. Rev.*, 75, 1169, doi: [10.1103/PhysRev.75.1169](https://doi.org/10.1103/PhysRev.75.1169)
- Frenkel, D., & Smit, B. 2001, *Understanding Molecular Simulation*, 2nd edn. (USA: Academic Press, Inc.)
- Gaisser, T. K. 2006, *Journal of Physics: Conference Series*, 47, 15, doi: [10.1088/1742-6596/47/1/002](https://doi.org/10.1088/1742-6596/47/1/002)
- Gallant, Y. A. 2002, *Particle Acceleration at Relativistic Shocks*. <https://arxiv.org/abs/astro-ph/0201243>
- Kirk, J. 2005, in *Hot Spots in Extragalactic Radio Sources: Proceedings of a Workshop Held at Ringberg Castle, Tegernsee, FRG, February 8–12, 1988*, Springer, 241–246
- Kirk, J. G., & Dendy, R. O. 2001, *Journal of Physics G Nuclear Physics*, 27, 1589, doi: [10.1088/0954-3899/27/7/316](https://doi.org/10.1088/0954-3899/27/7/316)
- Kirk, J. G., & Duffy, P. 1999, *Journal of Physics G: Nuclear and Particle Physics*, 25, R163, doi: [10.1088/0954-3899/25/8/201](https://doi.org/10.1088/0954-3899/25/8/201)
- Kirk, J. G., & Schneider, P. 1987a, *The Astrophysical Journal*, 315, 425, doi: [10.1086/165147](https://doi.org/10.1086/165147)
- . 1987b, *The Astrophysical Journal*, 322, 256, doi: [10.1086/165720](https://doi.org/10.1086/165720)
- Krymskii, G. F. 1977, *Akademiia Nauk SSSR Doklady*, 234, 1306
- Landau, L. D., & Lifshitz, E. M. 1987, *Fluid Mechanics*, Second Edition: Volume 6 (Course of Theoretical Physics), 2nd edn., *Course of theoretical physics / by L. D. Landau and E. M. Lifshitz*, Vol. 6 (Pergamon Press). <https://www.elsevier.com/books/fluid-mechanics/landau/978-0-08-057073-0>
- Longair, M. 2011, *High Energy Astrophysics* (Third Edition) (Cambridge, UK: Cambridge University Press)
- Mallick, R., & Irfan, M. 2019, *Monthly Notices of the Royal Astronomical Society*, 485, 577, doi: [10.1093/mnras/stz454](https://doi.org/10.1093/mnras/stz454)
- Mallick, R., & Verma, A. 2022, *Journal of High Energy Astrophysics*, 36, 36, doi: <https://doi.org/10.1016/j.jheap.2022.07.005>
- Neronov, A., & Malyshev, D. 2015, arXiv preprint arXiv:1505.07601
- Neronov, Andrii, Malyshev, Denys, & Semikoz, Dmitri V. 2017, *A&A*, 606, A22, doi: [10.1051/0004-6361/201731149](https://doi.org/10.1051/0004-6361/201731149)
- Peacock, J. A. 1981, *Monthly Notices of the Royal Astronomical Society*, 196, 135, doi: [10.1093/mnras/196.2.135](https://doi.org/10.1093/mnras/196.2.135)
- Prishchep, V. L., & Ptuskin, V. S. 1981, *AZh*, 58, 779
- Rezzolla, L., & Zanotti, O. 2013, *Relativistic Hydrodynamics* (Oxford University Press)
- Risken, H. 1989, *The Fokker-Planck equation. Methods of solution and applications* (Springer Berlin, Heidelberg)
- Schure, K. M., Bell, A. R., O’C Drury, L., & Bykov, A. M. 2012, *SSRv*, 173, 491, doi: [10.1007/s11214-012-9871-7](https://doi.org/10.1007/s11214-012-9871-7)
- Verma, A., & Mallick, R. 2023, *Monthly Notices of the Royal Astronomical Society*, 522, 4801, doi: [10.1093/mnras/stad1245](https://doi.org/10.1093/mnras/stad1245)
- Yang, R.-z., de Oña Wilhelmi, E., & Aharonian, F. 2014, *A&A*, 566, A142, doi: [10.1051/0004-6361/201321044](https://doi.org/10.1051/0004-6361/201321044)
- Yoon, Y. S., Ahn, H. S., Allison, P. S., et al. 2011, *ApJ*, 728, 122, doi: [10.1088/0004-637X/728/2/122](https://doi.org/10.1088/0004-637X/728/2/122)
- Yoon, Y. S., Anderson, T., Barrau, A., et al. 2017, *ApJ*, 839, 5, doi: [10.3847/1538-4357/aa68e4](https://doi.org/10.3847/1538-4357/aa68e4)
- Yuan, Q., Qiao, B.-Q., Guo, Y.-Q., Fan, Y.-Z., & Bi, X.-J. 2020, *FrPhy*, 16, 24501, doi: [10.1007/s11467-020-0990-4](https://doi.org/10.1007/s11467-020-0990-4)